Asymmetric Flexible MXene-Reduced Graphene Oxide Micro-Supercapacitor

Cedric Couly[1], Mohamed Alhabeb[1], Katherine L. Van Aken[1], Narendra Kurra[1,2], Luisa Gomes[1], Adriana M. Navarro-Suárez[1,3], Babak Anasori[1], Husam N. Alshareef[2], and Yury Gogotsi[1,]*

[1] A.J. Drexel Nanomaterials Institute, Department of Materials Science and Engineering, Drexel University, Philadelphia, PA 19104, USA
[2] Department of Materials Science and Engineering, King Abdullah University of Science and Technology (KAUST), Thuwal 23955-9600, Kingdom of Saudi Arabia
[3] CIC energiGUNE, Albert Einstein 48, 01510 Miñano, Alava, Spain
[*] E-mail: gogotsi@drexel.edu

Current microfabrication of micro-supercapacitors often involves multistep processing and delicate lithography protocols. In this study, simple fabrication of an asymmetric MXene-based micro-supercapacitor that is flexible, binder-free, and current-collector-free is reported. The interdigitated device architecture is fabricated using a custom-made mask and a scalable spray coating technique onto a flexible, transparent substrate. The electrode materials are comprised of titanium carbide MXene ($Ti_3C_2T_x$) and reduced graphene oxide (rGO), which are both 2D layered materials that contribute to the fast ion diffusion in the interdigitated electrode architecture. This MXene-based asymmetric micro-supercapacitor operates at a 1 V voltage window, while retaining 97% of the initial capacitance after ten thousand cycles, and exhibits an energy density of 8.6 mW h cm^{-3} at a power density of 0.2 W cm^{-3}. Further, these micro-supercapacitors show a high level of flexibility during mechanical bending. Utilizing the ability of $Ti_3C_2T_x$-MXene electrodes to operate at negative potentials in aqueous electrolytes, it is shown that using $Ti_3C_2T_x$ as a negative electrode and rGO as a positive one in asymmetric architectures is a promising strategy for increasing both energy and power densities of micro-supercapacitors.

1. Introduction

The miniaturization of microelectronic devices and the emergence of smart autonomous systems for a variety of applications, such as wearable sensors and "Internet of Things," require the development of integrated on-chip storage solutions.[1–3] As a result, developing flexible devices that can provide the required power to these electronic units, microsensors, and nanorobots has become very important.[2,3] Currently, thin-film or microbatteries are used for small scale energy storage, but they often suffer from low power density and limited cycle-life.[3–5] In this scenario, micro-electrochemical capacitors, also called micro-supercapacitors (MSCs), can offer a higher power density and a longer cycle life than batteries due to rapid electron–ion kinetics and sustainable electrode materials. The interdigitated coplanar electrode setup (that is, electrodes being in the same plane) allows for fast electrolyte ion diffusion between 2D sheets, when compared to cofacial sandwich geometry (that is, electrodes being stacked sequentially along with the separator).[2–4,6] Technically, interdigitated coplanar electrode architectures tend to exhibit a better electrochemical performance in terms of rate capability and power density over their sandwich counterparts.[7] Aside from electrode layout, the choice of electrode material plays a significant role in the resulting electrochemical performance.

In recent years, several fabrication schemes have been employed and many electrode materials were explored in fabricating state-of-the-art MSCs. Carbon based MSCs have been fabricated using activated carbon,[8] carbide derived carbon,[7,9] onion-like carbon,[10] carbon nanotubes,[11] and graphene.[12] Further, several micro-pseudocapacitors employing materials such as transition metal oxides (MnO_2)[13,14] and conducting polymers such as polyaniline, polypyrrole, and poly(3,4-ethylenedioxythiophene)[15–17] have also been reported. However, many of these MSCs fabrication methods require conventional photolithography, which involves the use of photomasks and microfabrication in a sophisticated cleanroom environment.[8,9,11–17] In order to avoid the use of such multistep processing which is complex and expensive, direct write methods have been proposed to fabricate MSCs.[18,19]

Among direct write methods, laser based techniques offer an easy fabrication method for MSCs. For example, EI-Kady and Kaner have demonstrated scalable fabrication of reduced graphene

oxide (rGO) MSCs by using laser scribing.[20] In another study, a symmetric interdigitated micro-supercapacitor was constructed by laser cutting of an rGO film.[21] However, rGO based symmetric devices have a limited areal capacitance (0.08–0.5 mF cm^{-2} and a typical thickness is in the range of 1 μm) due to its low electronic conductivity (15–30 S cm^{-1}), so pairing it with a more conductive material can improve the overall device performance.[11,18,22–24] Recently, our group fabricated current collector-free $Ti_3C_2T_x$ MXene MSCs employing a spray-coating method followed by a direct laser cutting process.[25] $Ti_3C_2T_x$-MXene, which has a hydrophilic surface,[26] exhibits metallic conductivity (≈6700 S cm^{-1})[27] which facilitates transfer of electrons and thus eliminates the need for noble metal current collectors.[25] Additionally, larger packing density, up to ≈4.0 g cm^{-3}, makes $Ti_3C_2T_x$-MXene a promising electrode for volumetric energy storage applications.[28,29] In aqueous electrolytes, $Ti_3C_2T_x$-MXene symmetric MSCs have a limited voltage window (≈0.6 V)[19,25] because $Ti_3C_2T_x$-MXene tends to be oxidized at high anodic potentials (for example, ≈0.8 V in a symmetric 2-electrode configuration).[25] To avoid the voltage window limitation associated with $Ti_3C_2T_x$-MXene as a positive electrode, an asymmetric electrode design can potentially widen the voltage window, leading to a MSC with the ability to operate at higher energy densities.[30]

In this study, we combined rGO and highly conductive $Ti_3C_2T_x$-MXene to make an asymmetric interdigitated MSC for the first time. These asymmetric MSCs are binder and current collector free, in contrast to most of the MSCs reported in literature.[2,3] By simple sequential spray coating of MXene and rGO using a custom-made mask, we fabricated asymmetric 2D MSCs without the use of photolithography. We also made a symmetric interdigitated $Ti_3C_2T_x$-MXene MSC using the same sequential spray coating process. Additionally, to explore the advantage of interdigitated design, we fabricated an asymmetric sandwich-type MSC comprised of spray-coated rGO and $Ti_3C_2T_x$. The asymmetric MSC shows a high degree of flexibility even after bending and twisting to 90°, withstanding 10,000 charge–discharge cycles as well as exhibiting better capacitance retention when compared to the symmetric device design. This prolonged cycling confirms that the electrodes in asymmetric architecture (both interdigitated and sandwich) maintain their layered structure without any chemical or physical degradation.

The fabrication protocol of asymmetric interdigitated MSCs is shown in Figure S1 in the Supporting Information. Both $Ti_3C_2T_x$ and rGO dispersions were sprayed onto a transparent

flexible polyethylene terephthalate (PET) substrate. We have used a hot air gun to dry each sprayed layer completely while suppressing the coffee ring effect in order to obtain uniform coatings. The challenging task in the coating process was to spray two different materials separately to make asymmetric interdigitated electrodes. To achieve this goal, we used a mask designed by direct laser engraving of the comb pattern on a Kapton film (Figure S2, Supporting Information). To make the mask adhere firmly onto the substrate, we used hair pins to hold the mask fingers down during spray coating of the electrode materials (Figure S2d, Supporting Information). First, a colloidal solution of rGO in ethanol (0.8 mg mL^{-1}) was sprayed over one of the Kapton mask patterns on the PET substrate, while simultaneously being dried with a hot air gun. Following this, the first Kapton mask was replaced by the second one, which covered the sprayed rGO fingers as well as the interspace between the two sets of finger electrodes (Figure S2, Supporting Information). Then $Ti_3C_2T_x$-MXene dispersion (1.0 mg mL^{-1}) was then sprayed and the outcome was an interdigitated electrode design of rGO and $Ti_3C_2T_x$ materials. A polyvinylalcohol (PVA)/H_2SO_4 gel electrolyte was carefully drop-casted onto the electrodes and left in air overnight at room temperature to dry completely. Finally, copper tape was attached at the edges of the two electrodes to connect to the potentiostat leads for testing (Figure S1, Supporting Information).

2. Results and Discussion

Electrode architecture and device configuration are important for maximizing the electrochemical performance of the chosen electrode materials. We have designed two device configurations, namely a sandwich (cofacial) and an interdigitated (coplanar) layout of 2D layers of rGO and $Ti_3C_2T_x$ as shown in **Figure 1**. In the interdigitated configuration, MXene and rGO layers are in the same plane (Figure 1a), whereas in the sandwich configuration, MXene and rGO layers face each other (Figure 1b).

We measured electrical conductivities of the spray-coated $Ti_3C_2T_x$ and rGO films by the four-point probe method at room temperature to be 6400 $\pm$ 120 and ≈10 S cm^{-1}, respectively (**Figure 2**a). The film thicknesses were about 300 nm, which is the film thickness of all the samples tested in this study. It is noteworthy that the electrical conductivity of $Ti_3C_2T_x$-MXene films is highly dependent on the flake size and flake-to-flake contact resistance at a given

thickness.[31] Indeed, it is possible to spray semi-transparent films of MXenes (<100 nm) as shown in Figure S3, Supporting Information. The homogenous nature of the spray-coated film allows one of Drexel University's building to be photographed through the MXene film (Figure S3a, Supporting Information). This demonstrates that $Ti_3C_2T_x$-MXene can be even potential candidate for transparent MSCs (Figure S3b, Supporting Information). However, thin MXene films (<100 nm) are prone to undergo oxidation in air and may require a coating to improve their stability.[31,32] Such thin films should be used in inert atmosphere with nonaqueous electrolyte to ensure the long term stability of MXene based devices.[30] As a result, for this study we used thicker coatings (≈300 nm) to demonstrate the feasibility of $Ti_3C_2T_x$-MXene. Figure 2b shows the crystallinity of spray-coated $Ti_3C_2T_x$-MXene and rGO films measured by X-ray diffraction (XRD). The (002) peaks of $Ti_3C_2T_x$-MXene and rGO are located at ≈7° and 23.8° (Figure 2b; Figure S4, Supporting Information), corresponding to d-spacing values of 12.62 and 3.88 Å, respectively. As for $Ti_3C_2T_x$-MXene, the interlayer spacing is attributed to two layers of intercalated water molecules.[33,34] The intense diffraction peaks of the PET substrate at 22.9° and 25.8° (Figure 2b) coincide with the broad (002) peak position of rGO which is around 23.82° (Figure S4a, Supporting Information). A scanning electron microscope (SEM) micrograph of the sprayed rGO is shown in Figure S4b (Supporting Information), which exhibits restacked graphene layers and uniform coatings across the region.

We then used Raman analysis to study the quality of MXene and rGO films as shown in Figure 2c. The Raman spectrum of $Ti_3C_2T_x$-MXene has a sharp peak at 200 cm^{-1} and broad peaks at 374 and 619 cm^{-1}, which are signatures of the $Ti_3C_2T_x$-MXene.[30] This shows that MXene preserves its structural characteristics after spraying into thin film form under hot air gun drying. On the other hand, Raman spectrum of rGO shows D and G bands centered around 1331 and 1592 cm^{-1} with full width half maximum (FWHM) of 109 and 85 cm^{-1}, respectively. The D band is due to defects and is related to zone boundary κ-point phonons with A1g symmetry.[35] Physical interpretation is related to breathing of polyaromatic carbon atoms, and the activation process is governed by electron–phonon interaction channeled by defects. The G band corresponds to collective symmetric stretching of sp^2 carbon lattice with E_{2g} symmetry.[35–37] The ratio of D-band intensity to G-band intensity (I_D/I_G) in Figure 2c is about 1.33, from which we can estimate the corresponding sp^2 crystallite size to be 9.2 nm using the following formula[35]:

$$L_a(\text{nm}) = 560/E_{\text{laser}}^4(I_D/I_G)^{-1} \quad (1)$$

where E_{laser} is the laser excitation energy in eV and L_a is the average sp^2 crystallite size.

Figure 3a shows a digital photograph of the as-fabricated 14-finger MSC device. Zooming in on the fingers allows us to distinguish the different colors of the electrodes (Figure 3b). Giving that $Ti_3C_2T_x$-MXene has a higher density than rGO, $Ti_3C_2T_x$ is brighter than the rGO films for the same amount of mass sprayed per area. Furthermore, we can clearly see the well-defined pattern of the electrode with a homogeneous spacing, which demonstrates the effectiveness of our simple fabrication process. To measure the interfinger spacing and the width of the fingers, a top-view SEM image of our 14-finger MSC was obtained (Figure 3d). The SEM image shows interfinger spacing of ≈ 400 μm and a finger width of ≈ 900 μm. The resolution limit of the spray coating process may depend on the type of the mask design used for the fabrication. In our study, the width and length of the electrodes are limited by the hard mask used to fabricate the asymmetric micro-supercapacitors. However, it is possible to achieve desired feature dimensions through photolithography or electron beam lithography techniques in combination with a spray coating process. The thickness is measured from the SEM cross section to be around 300 nm (Figure 3c, bottom). These thin electrodes are unique because they can be used without any current collectors either on top or bottom. This is in contrast to other MSCs, which typically use current collectors.[8–12]

We then tested the electrochemical performance of the MSC in two-electrode configuration using $Ti_3C_2T_x$-MXene and rGO as the negative and positive electrodes, respectively. We drop casted PVA/H_2SO_4 gel electrolyte onto the electrodes and left it in air overnight at room temperature to dry completely (Figure S1, Supporting Information). Cyclic voltammetry (CV) of the asymmetric MSC is shown in **Figure 4**a. It can be observed that the MSC operates at a voltage window of 1 V with a rectangular CV shape, indicating a good capacitive behavior of the two electrode materials. At 2 mV s^{-1}, the areal capacitance of the device was calculated to be around 2.4 mF cm^{-2} and the corresponding volumetric capacitance was estimated to be 80 F cm^{-3}. As summarized in Table S1 (Supporting Information), this areal capacitance is higher than values previously reported of comparable voltage window (≈1 V)[38,39] despite using thicker electrode (≈300 nm). Other symmetric MXene devices reported in literature are summarized in

Table S2 (Supporting Information), with more typical voltage windows of 0.6 V. Charge–discharge profiles of the asymmetric micro-supercapacitor are seen as slightly nonlinear, probably due to the pseudocapacitive nature of MXene electrode (Figure S5a, Supporting Information). The device has an equivalent series resistance value of 28 Ω, which is estimated from the high frequency region of the Nyquist plot as shown in Figure S5b (Supporting Information).

Using a silver wire pseudoreference in contact with the gel electrolyte,[40] we were able to distinguish the different performance of the two electrodes, as shown in Figure 4b. The even distribution of the cell voltage window could be seen, with the negative electrode ($Ti_3C_2T_x$) working from 0 to 0.5 V and the positive electrode (rGO) working from 0.5 to 1 V. This CV measurement was done at a low scan rate of 2 mV s^{-1} so the reduction of the $Ti_3C_2T_x$ at 0 V and the oxidation of the rGO at 1 V could be seen (Figure 4c). When we tested the symmetric $Ti_3C_2T_x$ interdigitated MSC, a maximum voltage window of 0.6 V was possible, which confirms the narrow voltage window of the symmetric configuration shown previously.[25] These results confirm that the total potential window can be increased to 1 V by using rGO as the positive electrode. Having an extended voltage window, the asymmetric interdigitated MSC showed a better energy density than the symmetric one at similar power densities (Figure 4d). It should be noted that at high scan rates, the symmetric device is slightly better than the asymmetric one. This can be due to the higher electronic conductivity of MXene compared to rGO, which causes the all-MXene symmetric device to have a higher rate capability (Figure S6, Supporting Information).

To better understand the benefit of an interdigitated (coplanar) electrode architecture compared to the sandwich (cofacial) electrode architecture explained at the beginning of this article, an asymmetric sandwich device was constructed with rGO//$Ti_3C_2T_x$. For consistency, the same amount of electrode material sprayed in the interdigitated setup was again sprayed for the sandwich configuration, allowing a fair comparison (Figure S7, Supporting Information). For the sandwich device, ≈300 nm films of $Ti_3C_2T_x$ and rGO were stacked on top of each other as shown in Figure S7c, Supporting Information. The Ragone plot clearly shows a sharp decrease in performance of the sandwich MSC at high scan rate, which can be attributed to the nonfavorable architecture of the sandwich configuration as explained in Figure 1.

Aside from their high surface area and high conductivity, 2D nanomaterials also boast a high flexibility, allowing bending and folding of the devices in any direction. Two plastic microscope slides were prepared to hold the MSC at a chosen angle while measuring CV curves. **Figure 5**a shows the MSC while held at 90° with the plastic microscope slides, using two hair pins to hold it. After being tested while bent at a variety of angles (0°, 30°, 60°, 90°, 120°, 180°) and twisted at 90°, our asymmetric interdigitated MSC maintained 100% of its capacitance value (Figure 5b). Thanks to the flexibility of the PET substrate, the MSC could easily be bent between fingers as shown on the background of Figure 5b. To the best of our knowledge, this is the first MSC that can be completely folded with no loss of performance.

A long cycling test has also been conducted, up to 10,000 cycles, while the same three MSCs (shown on the Ragone plot) were bent at 30° angle and charged at 0.2 mA cm^{-2}. When rGO was used as the positive electrode material in the interdigitated design, 97% of the capacitance was retained after 10,000 cycles (Figure 5c). The sandwich device shows similar capacitance retention (95%), while the capacitance of the all-MXene symmetric interdigitated device fades down to 75% after 10,000 cycles as a result of electrochemical oxidation. To confirm the excellent long cycling behavior, after the 10,000 cycles, XRD analysis was performed on the asymmetric interdigitated MSC. The XRD pattern of the $Ti_3C_2T_x$-MXene electrode after prolonged cycling (Figure 5d) has similar peaks to the as fabricated electrode (Figure 1c, top pattern). This confirms the durability of $Ti_3C_2T_x$-MXene when used as a negative electrode in asymmetric configurations. The (002) peak of MXene shows lower intensity, broadens and shifts from 7° to 5.8° after cycling as shown in Figure 5d, possibly due to intercalated PVA gel electrolyte that leads to swelling of MXene layers and interrupting MXene flakes restacking.[28,41] However, there are no signatures for TiO_2 formation observed after prolonged electrochemical testing. This is a clear indication that MXene can be exploited in the negative potential window in asymmetric devices, avoiding possible electrochemical oxidation that occurs in the symmetric configuration. Thus, the asymmetric design not only improves the electrochemical performance but also ensures the chemical stability of electrodes due to complementary potential window operation. The robustness of both layered materials in their respective voltage windows is reflected in the highly stable performance of the asymmetric MSCs.

3. Conclusion

In summary, we have demonstrated the fabrication of an asymmetric MXene-based interdigitated micro-supercapacitor by spray-coating onto a flexible PET substrate. The resulting device is binder-free, current-collector-free, flexible, and operates at a larger potential window than its symmetric counterpart. The resulting device successfully operates in an extended 1 V window, maintains its performance over ten thousand cycles, and exhibits an energy density of 8.6 mW h cm^{-3} at a power density of 0.2 W cm^{-3}. This study reveals the capability of $Ti_3C_2T_x$-MXene to operate at high cathodic voltages in aqueous electrolytes, which opens the door for designing asymmetric MSCs with high energy densities.

4. Experimental Section

Preparation of Ti_3AlC_2 MAX and $Ti_3C_2T_x$ MXene: The Ti_3AlC_2 MAX phase was synthesized as described by Naguib et al.[39] using Ti_2AlC (Kanthal, Sweden) and TiC (Sigma Aldrich) as precursors. The resulting loosely held compact powder was crushed and sieved to obtain Ti_3AlC_2 powder with particle size <40 μm. Titanium carbide ($Ti_3C_2T_x$) MXene was synthesized by selective etching of aluminum from Ti_3AlC_2 (<400 mesh size) and delaminating it using minimally intensive layer delamination (MILD) method.[26,32] Briefly, 1.0 g of Ti_3AlC_2 was added slowly to an etchant solution prepared by dissolving 1 g of lithium fluoride (LiF, Sigma-Aldrich) in 20 mL of 9 m hydrochloric acid (HCl, Sigma Aldrich). The reaction was allowed to proceed for 24 h at 35 °C. The acidic product was washed with deionized water (DI H_2O) via centrifugation at 3500 rpm for 5 min per cycle, decanting the water-like supernatant. These washing cycles were repeated till a stable dark-green supernatant was obtained, accompanied by noticeable swelling of the sediment into a jelly-like material. At this point, this jelly-like sediment was redispersed in 50 mL of DI H_2O and centrifuged for 5 min at 3500 rpm. The ink-like supernatant (5 mg mL^{-1}) was collected and further used for spray coating.

Preparation of GO and rGO: Graphite oxide was prepared using purified graphite (SP-1, Bay Carbon) following Hummer's method.[43] A 5 mg mL^{-1} colloidal dispersion of graphene oxide (GO) was made by ultrasonication of GO in DI H_2O (FB-505, Fischer Scientific, operating at 20 KHz and 500 W) for 1 h followed by centrifugation for 1 h at 3500 rpm, and collection of the supernatant. To prepare rGO, 10 mL aqueous ammonia (Alfa Aesar) was stirred with 50 mL of

GO in a Pyrex-flask and the temperature was brought to 90 °C before adding 5 mL of hydrazine monohydrate (Sigma-Aldrich).[44] The reaction was allowed to proceed for 1 h. The as prepared rGO was washed copiously with DI H_2O, collected, and then dried in a vacuum oven at 70 °C. 80 mg of rGO powder was dispersed via ultrasonication in 100 mL of ethanol and this suspension was used for spray-coating.

Preparation of PVA/H_2SO_4: 1 g PVA (Alfa Aesar, 98%) was dissolved in 10 mL DI H_2O at 85 °C for 4 h at which the transparent gel is achieved.[25] 1 g (0.84 mL) of concentrated sulfuric acid (Alfa Aesar) was added to 10 wt% PVA gel and stirred for 30 min to obtain 1 m PVA/H_2SO_4.

Fabrication of the Kapton Mask: Kapton sheets with a thickness of 5-mil (127 μm) were purchased from Cole-Palmer. Two separate comb-type masks (7.6 × 2.6 cm) were cut using a 10.6 μm 40 W CO_2 laser (Epilog Mini/Helix 8000, Epilog Laser, USA) with pulse duration of 14 μs. Vectoral cutting at 5.1 cm focal distance with 31% speed and 4% power was utilized as the standard laser setting during the mask production. AutoCAD technical drawing software was used to design the masks and communicate with the laser software. Optimal laser settings for the best mask cut were determined through a parametric study.

Fabrication of Asymmetric Micro-supercapacitor (All Detailed): A PET sheet was cut, cleaned with water and ethanol, and then taped onto a plastic microscope slide. Then the first Kapton mask was pinned down with hair pins previously cut and filed down for a perfect match with our set-up. The first colloidal suspension (rGO) was sprayed with a low cost ($20) spray-gun, and a hot air gun was used to dry the layers of deposited material after each spray (Figure S1a, Supporting Information). When the first spray was finished, the hair pins were carefully removed (Figure S1b, Supporting Information) and the first Kapton mask was replaced with the second one, which covered the sprayed rGO pattern as well as what would become the interspace between the two electrode materials. The second material ($Ti_3C_2T_x$) was sprayed using the same process (Figure S1c, Supporting Information). Once the second spray coat was done, the hair pins were removed and then the second Kapton mask was taken off, leaving the two electrodes as shown in Figure S1d (Supporting Information). The two sprayed electrode masses were calculated to be around 100 μg cm^{-2}. A razor blade was passed between the electrodes to avoid

any short circuits, shown in Figure 3d as a line made by the blade. Then, the PVA/H_2SO_4 electrolyte was dropped onto the device and left to dry overnight in air (Figure S1e, Supporting Information). Copper tape was then placed alongside each one of the electrode with no contact with the gel electrolyte (Figure S1f, Supporting Information). The final asymmetric interdigitated MSC was obtained as in Figure 3a. This same process was repeated for the symmetric interdigitated MSC replacing the sprayed rGO step with $Ti_3C_2T_x$ instead. Since the thickness of the electrodes used in this study was in sub-micrometer dimensions, these were referred as micro-supercapacitors.

Material Characterization: The morphology of the MXene sheets was imaged using a SEM (Zeiss Supra 50VP, Germany). The electrical conductivities of spray coated $Ti_3C_2T_x$ MXene and rGO films were measured using a four-point probe (ResTest v1, Jandel Engineering Ltd., Bedfordshire, UK) with a probe distance of 1 mm. The XRD patterns were measured by a powder diffractometer (Rigaku Smart Lab, USA) with Cu Kα radiation at a step size of 0.02° with 0.5 s dwelling time. Raman spectra were recorded using a Renishaw Raman microscope with LEICA CTR6000 setup with 633 nm laser, 1800 lines mm^{-1} grating with 10% focused laser beam. Spectra were collected with a dwell time of 60 s and for three accumulations. The thickness of electrodes was measured by an Optical Profilometer (Zygo New View 6000) and cross-sectional SEM.

Acknowledgements

The authors acknowledge Kathleen Maleski for designing the mask structure with AutoCAD and Bilen Akuzum for laser cutting of Kapton sheets. The authors also acknowledge Leah Clark for the schematic design. Material synthesis and electrochemical characterization work of M.A. and K.L.V.A. were funded by the Fluid Interface Reactions, Structures and Transport (FIRST) Center, an Energy Frontier Research Center funded by the U.S. Department of Energy, Office of Science, Office of Basic Energy Sciences. Research reported in this publication was partially supported by King Abdullah University of Science and Technology (KAUST). C.C. was supported by the Erasmus Mundus joint master program, Materials for Energy Storage and Conversion (M.E.S.C.). A.M.N-S. was supported by CIC energiGUNE, the Basque Government Scholarship for predoctoral formation (PRE_2015_2_0096) and the Egonlabur Traveling Grant

(EP_2016_1_0030). XRD and SEM were performed at the Centralized Research Facilities (CRF) at Drexel University.

References

[1] Z. L. Wang, *Nano Today* 2010, *5*, 512.

[2] M. Beidaghi, Y. Gogotsi, *Energy Environ. Sci.* 2014, *7*, 867.

[3] N. A. Kyeremateng, T. Brousse, D. Pech, *Nat. Nanotechnol.* 2017, *12*, 7.

[4] G. Xiong, C. Meng, R. G. Reifenberger, P. P. Irazoqui, T. S. Fisher, *Electroanalysis* 2014, *26*, 30.

[5] B. Mendoza-Sanchez, Y. Gogotsi, *Adv. Mater.* 2016, *28*, 6104.

[6] D. R. Rolison, J. W. Long, J. C. Lytle, A. E. Fischer, C. P. Rhodes, T. M. McEvoy, M. E. Bourg, A. M. Lubers, *Chem. Soc. Rev.* 2009, *38*, 226.

[7] P. Huang, C. Lethien, S. Pinaud, K. Brousse, R. Laloo, V. Turq, M. Respaud, A. Demortière, B. Daffos, P. L. Taberna, B. Chaudret, Y. Gogotsi, P. Simon, *Science* 2016, *351*, 691.

[8] D. Pech, M. Brunet, P.-L. Taberna, P. Simon, N. Fabre, F. Mesnilgrente, V. Conédéra, H. Durou, *J. Power Sources* 2010, *195*, 1266.

[9] J. Chmiola, C. Largeot, P.-L. Taberna, P. Simon, Y. Gogotsi, *Science* 2010, *328*, 480.

[10] D. Pech, M. Brunet, H. Durou, P. Huang, V. Mochalin, Y. Gogotsi, P.-L. Taberna, P. Simon, *Nat. Nanotechnol.* 2010, *5*, 651.

[11] X. Xiao, T. Li, Z. Peng, H. Jin, Q. Zhong, Q. Hu, B. Yao, Q. Luo, C. Zhang, L. Gong, J. Chen, Y. Gogotsi, J. Zhou, *Nano Energy* 2014, *6*, 1.

[12] Z. S. Wu, K. Parvez, X. Feng, K. Müllen, *Nat. Commun.* 2013, *4*, 2487.

[13] N. Kurra, Q. Jiang, H. N. Alshareef, *Nano Energy* 2015, *16*, 1.

[14] N. Kurra, N. A. Alhebshi, H. N. Alshareef, *Adv. Energy Mater.* 2015, *5*, 1401303.

[15] C. Meng, J. Maeng, S. W. M. John, P. P. Irazoqui, *Adv. Energy Mater.* 2014, *4*, 1301269.

[16] N. Kurra, Q. Jiang, A. Syed, C. Xia, H. N. Alshareef, *ACS Appl. Mater. Interfaces* 2016, *8*, 12748.

[17] Q. Jiang, N. Kurra, H. N. Alshareef, *Adv. Funct. Mater.* 2015, *25*, 4976.

[18] W. Gao, N. Singh, L. Song, Z. Liu, A. L. M. Reddy, L. Ci, R. Vajtai, Q. Zhang, B. Wei, P. M. Ajayan, *Nat. Nanotechnol.* 2011, *6*, 496.

[19] N. Kurra, B. Ahmed, Y. Gogotsi, H. N. Alshareef, *Adv. Energy Mater.* 2016, *6*, 1601372.

[20] M. F. El-Kady, R. B. Kaner, *Nat. Commun.* 2013, *4*, 1475.

[21] M. Wu, Y. Li, B. Yao, J. Chen, C. Li, G. Shi, *J. Mater. Chem. A* 2016, *4*, 16213.

[22] Z.-S. Wu, K. Parvez, X. Feng, K. Mullen, *J. Mater. Chem. A* 2014, *2*, 8288.

[23] Z. Niu, L. Zhang, L. Liu, B. Zhu, H. Dong, X. Chen, *Adv. Mater.* 2013, *25*, 4035.

[24] J. J. Yoo, K. Balakrishnan, J. Huang, V. Meunier, B. G. Sumpter, A. Srivastava, M. Conway, A. L. Mohana Reddy, J. Yu, R. Vajtai, P. M. Ajayan, *Nano Lett.* 2011, *11*, 1423.

[25] Y.-Y. Peng, B. Akuzum, N. Kurra, M.-Q. Zhao, M. Alhabeb, B. Anasori, E. C. Kumbur, H. N. Alshareef, M.-D. Ger, Y. Gogotsi, *Energy Environ. Sci.* 2016, *9*, 2847.

[26] F. Shahzad, M. Alhabeb, C. B. Hatter, B. Anasori, S. M. Hong, C. M. Koo, Y. Gogotsi, *Science* 2016, *353*, 1137.

[27] X. Sang, Y. Xie, M.-W. Lin, M. Alhabeb, K. L. Van Aken, Y. Gogotsi, P. R. C. Kent, K. Xiao, R. R. Unocic, *ACS Nano* 2016, *10*, 9193.

[28] M. R. Lukatskaya, O. Mashtalir, C. E. Ren, Y. Dall'Agnese, P. Rozier, P. L. Taberna, M. Naguib, P. Simon, M. W. Barsoum, Y. Gogotsi, *Science* 2013, *341*, 1502.

[29] M. Ghidiu, M. R. Lukatskaya, M.-Q. Zhao, Y. Gogotsi, M. W. Barsoum, *Nature* 2014, *516*, 78.

[30] B. Anasori, M. R. Lukatskaya, Y. Gogotsi, *Nat. Rev. Mater.* 2017, *2*, 16098.

[31] A. D. Dillon, M. J. Ghidiu, A. L. Krick, J. Griggs, S. J. May, Y. Gogotsi, M. W. Barsoum, A. T. Fafarman, *Adv. Funct. Mater.* 2016, *26*, 4162.

[32] A. Lipatov, M. Alhabeb, M.R. Lukatskaya, A. Boson, Y. Gogotsi, A. Sinitskii, *Adv. Electron. Mater.* 2016, *2*, 1600255.

[33] Y. Dall'Agnese, P. Rozier, P. L. Taberna, Y. Gogotsi, P. Simon, *J. Power Sources* 2016, *306*, 510.

[34] H.-W. Wang, M. Naguib, K. Page, D. J. Wesolowski, Y. Gogotsi, *Chem. Mater.* 2016, *28*, 349.

[35] A. C. Ferrari, J. Robertson, *Phys. Rev. B* 2000, *61*, 14095.

[36] M. A. Pimenta, G. Dresselhaus, M. S. Dresselhaus, L. G. Cancado, A. Jorio, R. Saito, *Phys. Chem. Chem. Phys.* 2007, *9*, 1276.

[37] A. C. Forse, C. l. Merlet, P. K. Allan, E. K. Humphreys, J. M. Griffin, M. Aslan, M. Zeiger, V. Presser, Y. Gogotsi, C. P. Grey, *Chem. Mater.* 2015, *27*, 6848.

[38] W. Liu, X. Yan, J. Chen, Y. Feng, Q. Xue, *Nanoscale* 2013, *5*, 6053.

[39] M. Naguib, M. Kurtoglu, V. Presser, J. Lu, J. Niu, M. Heon, L. Hultman, Y. Gogotsi, M. W. Barsoum, *Adv. Mater.* 2011, *23*, 4248.

[40] K. L. Van Aken, M. Beidaghi, Y. Gogotsi, *Angew. Chem., Int. Ed. Engl.* 2015, *54*, 4806.

[41] Z. Ling, C. E. Ren, M. Q. Zhao, J. Yang, J. M. Giammarco, J. S. Qiu, M. W. Barsoum, Y. Gogotsi, *Proc. Natl. Acad. Sci. USA* 2014, *111*, 16676.

[42] W.-W. Liu, Y.-Q. Feng, X.-B. Yan, J.-T. Chen, Q.-J. Xue, *Adv. Funct. Mater.* 2013, *23*, 4111.

[43] W. S. Hummers, R. E. Offeman, *J. Am. Chem. Soc.* 1958, *80*, 1339.

[44] D. Li, M. B. Muller, S. Gilje, R. B. Kaner, G. G. Wallace, *Nat. Nanotechnol.* 2008, *3*, 101.

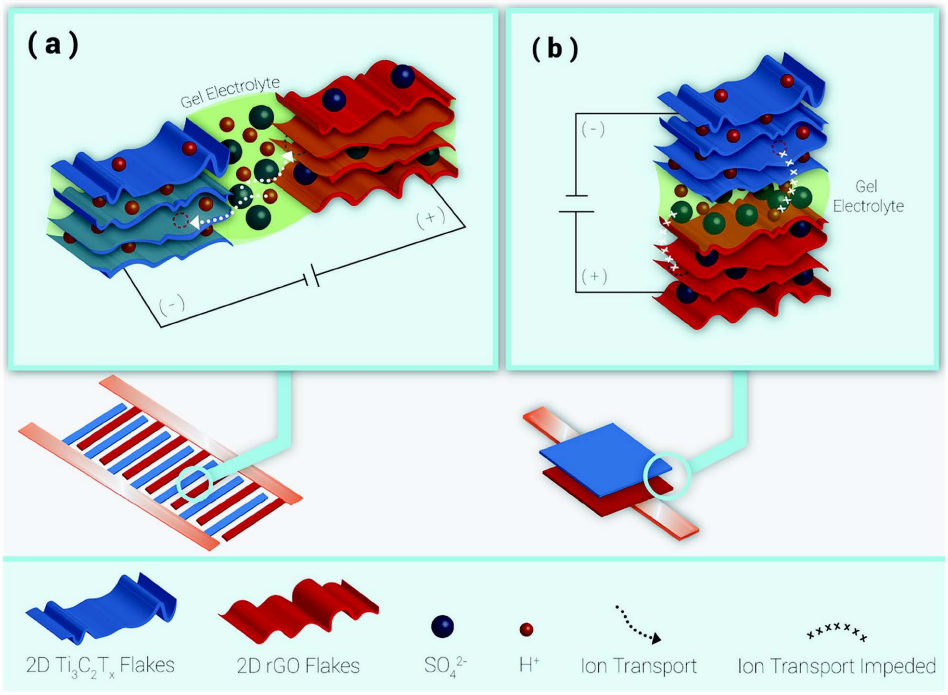

Figure 1. Schematic illustrations demonstrating a) interdigitated and b) sandwich configurations of asymmetric MSCs. The interdigitated architecture a) allows for facile in-plane diffusion of ions between electrodes while b) the sandwich architecture impedes ion transport pathways between the layers of the electrode materials. Device schematics shown here are used throughout article figures.

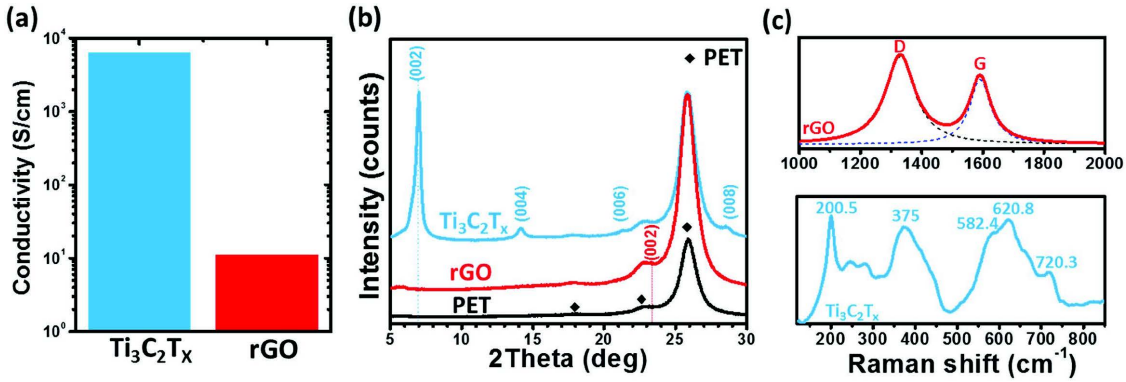

Figure 2. a) Electrical conductivities of spray coated $Ti_3C_2T_x$ and rGO films. b) XRD patterns and c) Raman spectra of $Ti_3C_2T_x$ and rGO films.

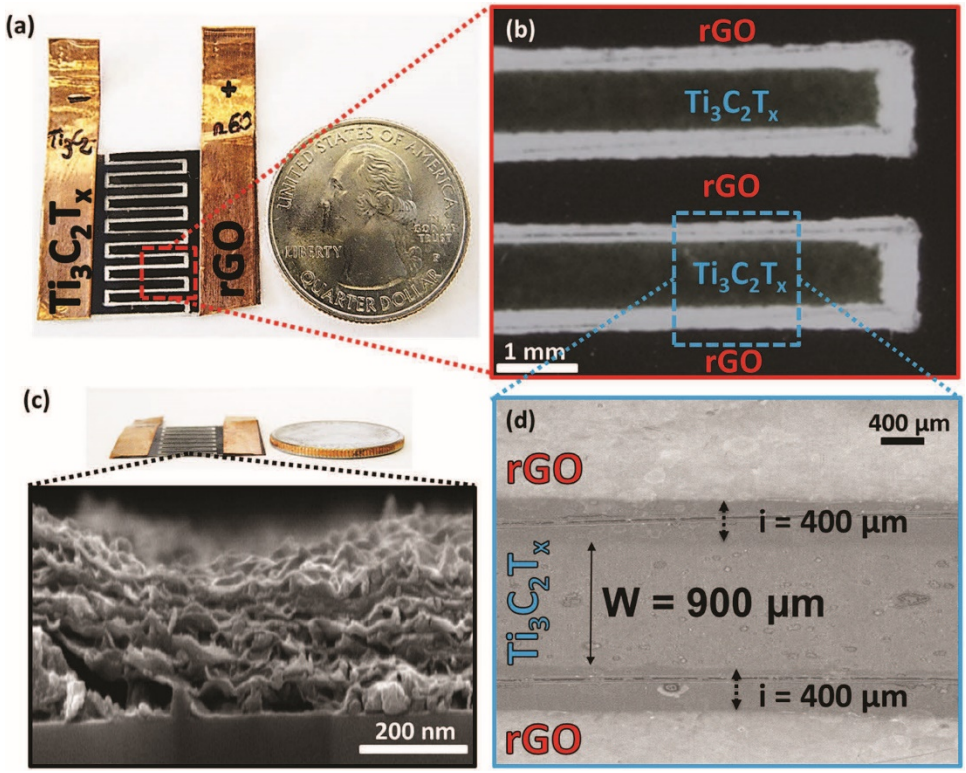

Figure 3. a) Digital photograph showing a top-view of the asymmetric MSC device along with a quarter U.S. dollar coin for size comparison, as well as a b) zoomed-in image of $Ti_3C_2T_x$ and rGO interdigitated electrode configurations and the interspace. c) Side view of the device with a U.S. quarter dollar coin and SEM cross-sectional image of the $Ti_3C_2T_x$ electrode. d) Top-view SEM image of the interdigitated fingers, showing one $Ti_3C_2T_x$ electrode between two rGO electrodes.

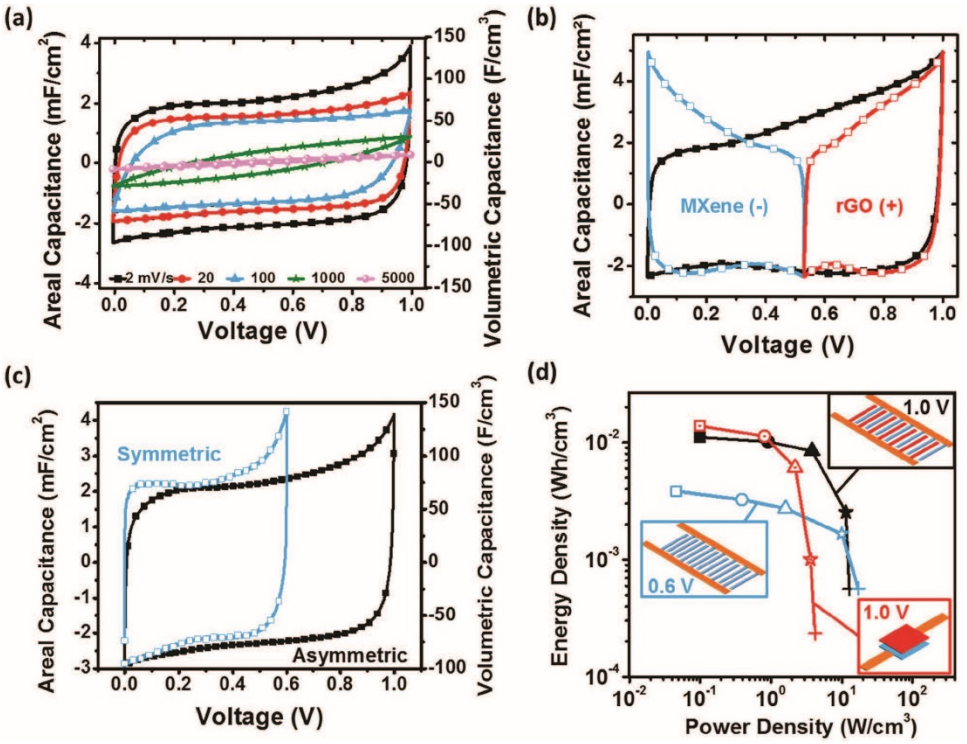

Figure 4. a) CVs of the asymmetric MSC at different scan rates (2–5000 mV s^{-1}) in a 2-electrode configuration. b) CVs of the MSC and the individual electrodes recorded at 2 mV s−1 in a 3-electrode configuration. c) Comparison between asymmetric interdigitated MSC and all-MXene symmetric interdigitated MSC at 2 mV s^{-1}. d) Ragone plot of asymmetric interdigitated MSC (Black, top right), asymmetric sandwich MSC (red, bottom right), and all-MXene symmetric interdigitated MSC (blue, middle left) with scan rates ranging between 2 and 5000 mV s^{-1}.

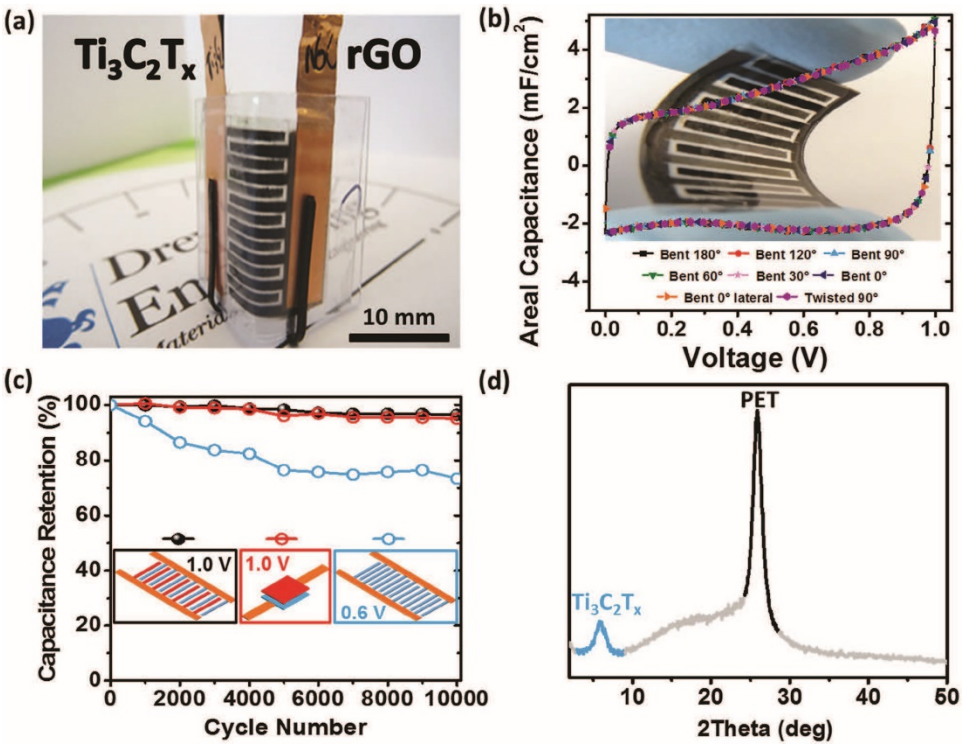

Figure 5. a) MSC with two microscope slides to hold it at 90° angle with two hair pins. b) CVs recorded at 2 mV s^{-1} while the device is bent and twisted at different angles. A flexible MSC without a current collector is shown in the background. c) Capacitance retention of the three different MSCs when cycled at 0.2 mA cm^{-2} while held at an angle of 30°. From the left to the right interdigitated asymmetric MSC (black), sandwich asymmetric MSC (red), and interdigitated symmetric MSC (blue). d) XRD of the asymmetric interdigitated MSC after 10,000 cycles.